IEEE Access
Multidisciplinary | Rapid Review | Open Access Journal

Received 21 January 2023, accepted 15 February 2023, date of publication 24 February 2023, date of current version 29 March 2023.

Digital Object Identifier 10.1109/ACCESS.2023.3248620

RESEARCH ARTICLE

Implementation of ZVS for Double-Sided LCC Inductive Coupled Wireless Power Transfer System Under Constant Current/Constant Voltage Operation Mode

DA LI[1], XUSHENG WU[1], CHUNYANG AN[1], JIANXIN GAO[2], AND WEI GAO[1]
[1]School of Electrical Engineering, Naval University of Engineering, Wuhan 430033, China
[2]National Key Laboratory of Science and Technology on Vessel Integrated Power System, Naval University of Engineering, Wuhan 430033, China

Corresponding author: Wei Gao (depkin@163.com)

This work was supported in part by the National Natural Science Foundation of China 51807197, and in part by the Innovation Group Talents Project of Hubei Natural Science Foundation under Grant 2018CFA008.

ABSTRACT The soft-switching characteristics of double-sided LCC wireless power transmission systems are susceptible to system parameter disturbances. In order to improve the stability of zero voltage switches in constant-current and constant-voltage charging modes, this paper synthesizes eight resonant conditions which make the system realize constant-current/constant-voltage and Zero Phase Angle. The influence of compensating capacitance parameter disturbance on system impedance angle is studied under constant current/constant voltage operation mode. The parameter configuration methods of compensated capacitance realized by zero voltage switches under the influence of third-order harmonic in constant current/constant voltage operation mode are also given. The system's experimental prototype verifies the theoretical analysis's accuracy with capacitive and inductive input impedance.

INDEX TERMS Wireless power transfer, constant current/constant voltage, double-sided LCC, zero-voltage-switch.

I. INTRODUCTION

Wireless power transfer has been widely used in the military, transportation, medical, and other fields due to its high safety, convenience, and flexibility [1], [2], [3], [4], [5]. Lithium batteries are applied in electric vehicle power batteries due to their high energy density, high cycle life, and low cost. During the charging process of lithium batteries, the equivalent load resistance changes from a few ohms to hundreds of ohms, so it is necessary to realize load-independent constant current (CC)/constant voltage (CV) charging in a wide range of loads. It is conducive to the safe and stable operation of electric vehicle power batteries, improving battery durability and maintaining stable working performance [6], [7], [8].

Load-independent CC/CV charging can be achieved by adding DC-DC converters or changing the system's operating frequency. However, adding DC-DC converters will increase devices, power loss, and cost of use, making it challenging to implement ZPA(Zero Phase Angle) or ZVS(Zero Voltage Switch) over the entire charging range [9], [10]. Due to the frequency bifurcation phenomenon, the frequency conversion control of the system will be unstable, leading to electromagnetic compatibility problems [11]. The frequency bifurcation phenomenon can be effectively avoided by adjusting the duty cycle, but it is challenging to realize ZVS under light load. Therefore, it is necessary to design specific resonant conditions for the IPT system and a set of resonant networks to achieve CC and CV output.

The traditional compensation method is based on SS, SP, PS, and PP models. The SS compensation network is independent of load and coupling coefficient, which can realize CC output independent of load, even if the transformer is damaged. The SP compensation network varies with the quadratic variation of the coupling coefficient, which can

The associate editor coordinating the review of this manuscript and approving it for publication was Zhixiang Zou.

realize load-independent CV output. The coupling coefficient and load resistance affect the PS and SP compensation networks [12], [13], [14]. In order to reduce the coil offset efficiency and power variation and to realize the CC/CV output and input ZPA characteristics. Adding an LC network to the transmitter or receiver can form the double-sided LCL, LCC-S, and LCC-P compensation network. LCC-S compensation network can achieve load-independent CV output and input ZPA characteristics; LCC-P and the double-sided LCL can achieve load-independent CC output and input ZPA characteristics. In the double-sided LCL compensation network, the compensation inductance is the same as the self-inductance of the coil [15], [16], [17]. Based on the disadvantage of low double-sided LCL Freedom, professor Chris Mi of San Diego State University proposed the double-sided LCC compensation network [9], [18]. The double-sided LCC compensation network not only has the advantages of the double-sided LCL but also reduces the value of compensation inductance and increases the design freedom of system parameters by adding additional compensation capacitance. The double-sided LCC compensation network has the strong anti-offset ability, can achieve CC output and input ZPA characteristics through parameter design, and can also achieve CV output and input ZPA characteristics. The IPT system of the double-sided LCC compensation network is a tangled resonant system, and it is too complicated to analyze the phase angle of the input port when CC/CV is performed directly on it. Prof. Xiaohui Qu and Van-Bin Vu analyzed the double-sided LCC compensation network using a two-port network and proposed a method to achieve load-independent CC and CV output at two ZPA frequencies [20], [21]. Nevertheless, there is no comprehensive analysis of all possible resonance conditions of the double-sided LCC compensation network. Voltage source full bridge inverter can reduce switching device stress and system loss when ZVS is realized. The double-sided LCC compensation network is a high-order resonant network. The difference between the actual parameters and the calculated matching parameters is inevitable in the experiment process, which leads to the loss of soft switching of the system. The existing solution is to design a larger inductive interval to counteract the loss of soft switching caused by load changes, but it will also increase reactive power. Therefore, it is necessary to systematically analyze the influence of the parameter disturbance of the compensation network on the system, thus contributing to the parameter design of the system. As for the series compensation capacitance parameters of the primary/secondary side are the main part of the resonant compensation for the primary/secondary side coil, and the parallel compensation capacitance parameters of the primary/secondary side are the main part of the resonant compensation for the compensation inductance parameters. Therefore, the compensation capacitor is also essential to the compensation network. Professor Wu Xusheng analyzed the disturbance of the double-sided LCC compensation network's primary and secondary series compensation capacitors and obtained the changes in the system's equivalent input impedance angle and output efficiency. The output performance is analyzed for the parameter offset of the series compensation capacitor, and the optimal capacitor configuration method is put forward on this basis, improving the anti-offset system performance [22]. The output sensitivity of constant current and constant voltage in the double-sided LCC compensation network at different operating frequencies is analyzed, and a parameter optimization method for compensation capacitors is proposed [23]. However, the influence of parameter disturbance of parallel compensation capacitors in double-sided LCC compensation networks on system characteristics and the acceptable range of parameter fluctuation of compensation capacitors for ZVS is not considered. For the double-sided LCC compensation network, the influence of compensation capacitance parameters on the system under CC/CV conditions and the allowable fluctuation range of compensation capacitance parameters for ZVS should be considered, respectively.

In this paper, Section II systematically analyzes the resonant conditions of eight double-sided LCC compensation networks to achieve CC and CV output and input ZPA and proposes a parameter design method to improve the system's anti-offset capability. Section III analyzes the impact of compensation capacitance parameter fluctuations on the system's output performance and impedance angle. Section IV establishes an experimental prototype to verify the experimental results of capacitive and inductive input impedance.

II. CASCADED EQUIVALENT AND RESONANT CONDITIONS OF DOUBLE-SIDED LCC COMPENSATION NETWORK

A. A NINTH-ORDER TWO-PORT MODEL OF DOUBLE-SIDED LCC

The leakage inductance T-type equivalent model of the double-sided LCC compensation network is a ninth-order two-port resonant network. The compensation inductance of the transmitter L_1, the reactance value of the parallel compensation capacitor C_1, and the series compensation capacitor C_p are divided into jx_1, jx_2, jx_3. In the Magnetizing inductance L_m, the receiving end is connected in series with the compensation capacitor C_s', and the reactance values of the parallel compensation capacitor C_2' and compensation inductance L_2' are divided into jx_4, jx_5, jx_6.

B. CASCADED EQUIVALENT AND RESONANT CONDITIONS OF DOUBLE-SIDED LCC COMPENSATION NETWORKS

A voltage source feeds the system to realize CC output, and CV-CC is converted an odd number of times. The last stage of the T-type resonant network is the cascade of second-order anti-L-type resonant network and first-order series network. The nine-order two-port network can be equivalent to the six-order two-port resonant network to realize the cascade of CV-CV and CV-CC T-type resonant networks. The third-order T-type resonant network can be cascaded equivalent to the first- and second-order resonant networks. Therefore,

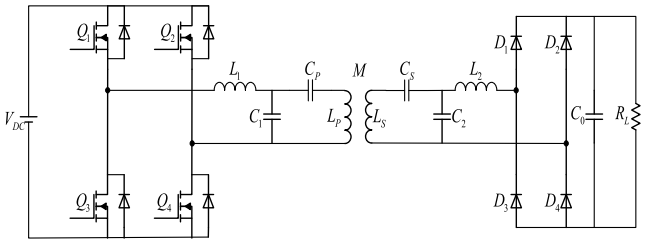

FIGURE 1. Double-sided LCC compensation topology.

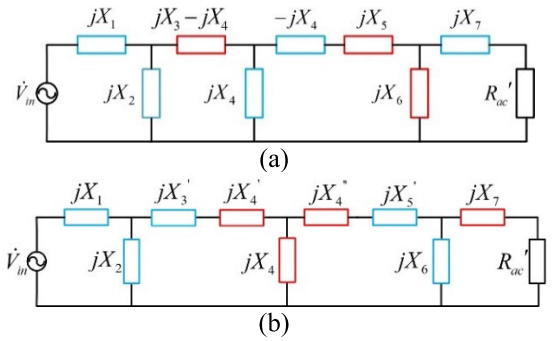

FIGURE 2. Cascaded equivalence of CC of the two-port resonant network.

there are two ways for the sixth-order two-port resonant network to realize CV-CV. It is equivalent to the cascade of the second-order anti-L-type resonant network, first-order series network, and second-order L-type resonant network. It is also equivalent to the cascade of two second-order anti-L-second order and L-type resonant networks, the cascade of two CV-CV T-type resonant networks [6]. The cascade equivalence of two ninth-order two-port resonant networks when realizing CV-CC is shown in Figure 2. The ninth-order two-port resonant network is equivalent to the network shown in Figure 2(a). The resonance conditions are in formula (1).

$$\begin{aligned} X_1 + X_2 &= 0 \\ X_5 + X_6 &= 0 \end{aligned} \tag{1}$$

The ninth-order two-port resonant network is equivalent to the network shown in Figure 2(b). And $jX_3' = jX_3 - ajX_4, jX_4' = (a-1)jX_4, jX_4'' = j(1/a-1)X_4, jX_5' = jX_5 - jX_4/a$, a is an unknown number. The resonance condition is in formula (2).

$$\begin{aligned} X_1X_2 + X_2X_3' + X_1X_3' &= 0 \\ X_4X_4' + X_4X_4'' + X_4'X_4'' &= 0 \\ X_5' + X_6 &= 0 \end{aligned} \tag{2}$$

$jX_3' = jX_3 - ajX_4, jX_4' = (a-1)jX_4, jX_4'' = j(1/a-1)X_4, jX_5' = jX_5 - jX_4/a$. The two-port resonant network is equivalent to the network in Figure 2(b). The resonance condition is

$$(X_3 + X_1X_2/(X_1+X_2))(X_5+X_6) = X_4^2 \tag{3}$$

The two-port resonant network realizes ZPA based on the CV-CC. The first-order T-type resonant network can be cascaded equivalent to the first-order series network and

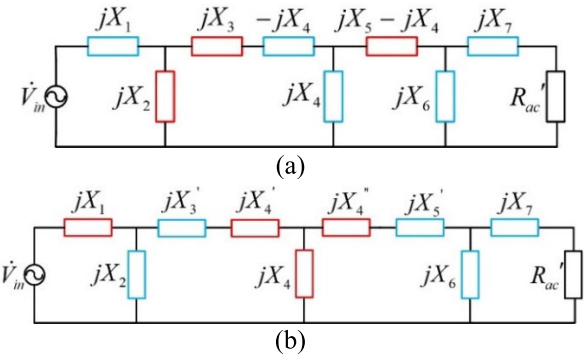

FIGURE 3. Cascaded equivalence of CC and ZPA of the two-port resonant network.

the second-order L-type resonant network to realize CC-CV. The remaining sixth-order two-port resonant network realizes CV-CV. There are two equivalents to the cascade of the sixth-order two-port resonant network. It is equivalent to the cascade of a second-order inverse L-type resonant network, a first-order series network, and a second-order L-type resonant network. It can also be equivalent to the cascade of two T-type resonant networks. Figure 3 shows the cascaded equivalent ways of two two-port resonant networks to achieve CV-CC and ZPA.

The ninth-order two-port resonant network is equivalent to the network shown in Figure 3(a). The resonance conditions are in formula (5).

$$\begin{aligned} X_2 + X_3 &= 0 \\ X_6 + X_7 &= 0 \end{aligned} \tag{4}$$

The ninth-order two-port resonant network is equivalent to the network shown in Figure 3(b). The resonance conditions are in the formula (4).

$$\begin{aligned} X_2 + X_3' &= 0 \\ X_4X_4' + X_4X_4'' + X_4'X_4'' &= 0 \\ X_5'X_6 + X_5'X_7 + X_6X_7 &= 0 \end{aligned} \tag{5}$$

$jX_3' = jX_3 - ajX_4, jX_4' = (a-1)jX_4, jX_4'' = j(1/a-1)X_4$, $jX_5' = jX_5 - jX_4/a$. Combine the three formulas of (4), and the ninth-order two-port resonant network is equivalent to the network in Figure 3(b). The resonance condition is

$$(X_5 + X_6X_7/(X_6+X_7))(X_2+X_3) = X_4^2 \tag{6}$$

The system has two resonance conditions from formulas (1) and (2) to realize CC output. From equations (3) and (4), the system has two resonance conditions of ZPA based on CV. The system has four resonance conditions to achieve CC and ZPA. The four sets of resonance conditions are in formula (6).

$$CC1: \begin{cases} X_1 + X_2 = 0 \\ X_5 + X_6 = 0 \\ X_2 + X_3 = 0 \\ X_6 + X_7 = 0 \end{cases}$$

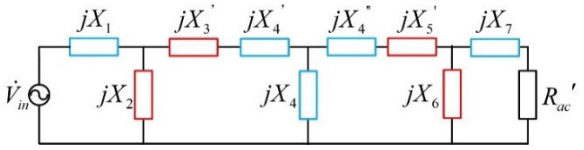

FIGURE 4. Cascaded equivalence of CV and ZPA of the two-port resonant network.

$$
\begin{aligned}
CC2:&\begin{cases} X_1+X_2=0 \\ X_5+X_6=0 \\ (X_5+(X_6X_7/X_6+X_7))(X_2+X_3)=X_4^2 \end{cases} \\
CC3:&\begin{cases} (X_3+(X_1X_2/X_1+X_2))(X_5+X_6)=X_4^2 \\ X_2+X_3=0 \\ X_6+X_7=0 \end{cases} \\
CC4:&\begin{cases} (X_3+(X_1X_2/X_1+X_2))(X_5+X_6)=X_4^2 \\ (X_5+(X_6X_7/X_6+X_7))(X_2+X_3)=X_4^2 \end{cases}
\end{aligned} \tag{7}
$$

The equivalent cascade analysis of CV-CV for the ninth-order two-port network is similar to the cascade equivalent analysis of CV-CV. Three low-level cascade equivalents realize CV-CV. It is equivalent to three cascades of T-type resonant networks that realize CV-CV. It is also equivalent to an anti-L-type resonant network, a series network, an L-type resonant network, and T-type resonant networks. It also can be equivalent to the cascade of a T-type resonant network, an L-type resonant network, a series network, and an L-type resonant network that realizes the CV-CV. Furthermore, a is an unknown number, $jX_3' = jX_3 - ajX_4$, $jX_4' = (a-1)jX_4$, $jX_4'' = j(1/a-1)X_4$, $jX_5' = jX_5 - jX_4/a$.

The ninth-order two-port resonant network realizes ZPA based on the CV-CV. The T-type resonant network of the first stage should be CC-CV. The cascade of the first-order series network, the second-order L-type resonant network, and the T-type resonant network of the last stage should be CV-CC. The first-order inverse L-type resonant network is a cascade of first-order series networks, and the middle-level T-type resonant network is CV-CV. The ninth-order two-port network realizes the cascading equivalent of ZPA based on CV-CV in Figure 4.

The ninth-order two-port resonant network equivalently cascaded is shown in Figure 4. The resonance conditions are in formula (7).

$$
\begin{aligned}
&X_2+X_3'=0 \\
&X_4X_4'+X_4X_4''+X_4'X_4''=0 \\
&X_5'+X_6=0
\end{aligned} \tag{8}
$$

The ninth-order two-port resonant network realizes the resonant condition of ZPA on the realization of CV-CV conversion shown in formula (8).

$$
(X_2+X_3)(X_5+X_6)=X_4^2 \tag{9}
$$

Three resonance conditions enable the double-sided LCC network to achieve CV-CV and ZPA in formula (9).

TABLE 1. Feasibility of resonance condition of the double-sided LCC compensation network.

Resonance condition	Feasibility	Resonance condition	Feasibility
$CC1-CV1$		$CC3-CV1$	
$CC1-CV2$		$CC3-CV2$	√
$CC1-CV3$	√	$CC3-CV3$	√
$CC2-CV1$	√	$CC4-CV1$	√
$CC2-CV2$		$CC4-CV2$	√
$CC2-CV3$	√	$CC4-CV1$	√

$$
\begin{aligned}
CV1:&\begin{cases} X_1X_2+X_1X_3+X_2X_3=0 \\ X_6+X_7=0 \\ (X_2+X_3)(X_5+X_6)=X_4^2 \end{cases} \\
CV2:&\begin{cases} X_5X_6+X_5X_7+X_6X_7=0 \\ X_1+X_2=0 \\ (X_2+X_3)(X_5+X_6)=X_4^2 \end{cases} \\
CV3:&\begin{cases} (X_3+\dfrac{X_1X_2}{X_1+X_2})(X_5+\dfrac{X_6X_7}{X_6+X_7})=X_4^2 \\ (X_2+X_3)(X_5+X_6)=X_4^2 \end{cases}
\end{aligned} \tag{10}
$$

C. FEASIBILITY ANALYSIS OF PARAMETRIC DESIGN METHOD

According to the above analysis, 12 resonance conditions enable the double-sided LCC compensation network to achieve CC and ZPA at one operating frequency; and achieve CV output and ZPA resonance conditions at another operating frequency. The feasibility and judgment of 12 resonance conditions are in Table 1. It can be seen from Table 1 that there are eight possible resonance conditions for the double-sided LCC compensation network. This paper gives the formulas of the parameter design method and the constraints of the compensation inductance ratio (the ratio of the compensation inductance to the self-inductance of the transmitting coil.

Furthermore, the ratio of the transmitter compensation inductance is ξ_1,the ratio of the receiver compensation inductance is ξ_2. It is found that the $CC3-CV3$ and $CC2-CV3$ parameter design methods are equivalent to the cascaded two-port resonant network at the CC operating frequency. Therefore, the parameter design equation $CC3-CV3$ is similar $CC2-CV3$. For the two-parameter design methods $CC3-CV2$ and $CC2-CV1$, the cascaded equivalent of the two-port resonant network at the CC operating frequency. It is also the cascaded equivalent of the two-port resonant network at the CV operating frequency. $CC4-CV2$ and $CC4-CV1$, the cascaded equivalent dual of a two-port resonant network at CV operating frequency. Therefore, the parameter design method $CC4-CV2$ is also similar to $CC4-CV1$. From the frequency characteristic curves of the transfer parameters of each parameter design method, eight parameter design methods can realize CC/CV output and ZPA. Through the parameter design equation in Table 3, it is found that

there are constraints between the compensation inductance ratio at the receiver and the compensation capacitance ratio at the transmitter of the eight parameter design methods, and the IPT system of the double-sided LCC compensation network can achieve CC/CV output and input ZPA. However, only the parameter design method $CC4-CV3$ has an additional degree of freedom. The parameter design method $CC4-CV3$ can also make the IPT system have the ability to resist offset under constant current/constant voltage operation mode, that is, when the coupling coefficient changes, the power change of the system under the same load is small.

D. SELECTION OF PARAMETER DESIGN METHOD

The parameter design method can promote the double-sided LCC compensation network and the anti-offset capability in CC/CV and ZPA. The power change of the system under the same load is small when the coupling coefficient is changed. The parametric design method $CC4-CV3$ can be solved by giving additional constraints against migration. Parameters A and B in the transfer parameter matrix of the system leakage inductance model in formula (11).

$$\begin{aligned} A &= \frac{X_1X_2+X_2X_3+X_1X_3}{X_2}\frac{X_5+X_6}{X_6}\frac{1}{X_4}-\frac{X_1+X_2}{X_2}\frac{1}{X_6}X_4 \\ B &= \frac{X_1X_2+X_2X_3+X_1X_3}{X_2}\frac{X_5X_6+X_5X_7+X_6X_7}{X_6X_4} \\ &\quad -\frac{X_1+X_2}{X_2}\frac{X_6+X_7}{X_6}X_4 \end{aligned} \tag{11}$$

The leakage inductance model parameters in formula (13) and the parameters in the transfer parameter matrix are converted into formula (12).

$$\begin{aligned} A &= m_A\frac{1}{k}-n_Ak \\ B &= m_B\frac{1}{k}-n_Bk \end{aligned} \tag{12}$$

The expression of m_A, n_A, m_B, n_B is shown in formula(15). X represents the reactance value of the self-inductance of the transmitter coil.

$$\begin{aligned} m_A &= \frac{X_1X_2+X_2X_3+X_1X_3}{X_2}\frac{X_5+X_6}{X_6}\frac{1}{X} \\ n_A &= \frac{X_1+X_2}{X_2}X \\ m_B &= \frac{X_1X_2+X_2X_3+X_1X_3}{X_2}\frac{X_5X_6+X_5X_7+X_6X_7}{X_6X_4}\frac{1}{X} \\ n_B &= \frac{X_1+X_2}{X_2}\frac{X_6+X_7}{X_6}X \end{aligned} \tag{13}$$

The load is R, the output power is

$$P_{out} = \frac{V_{in}^2}{A^2R'_{ac}+\frac{B^2}{R'_{ac}}} \tag{14}$$

Derive the coupling coefficient from formula (13) to get

$$\begin{aligned} \frac{\partial P_{out}}{\partial k} &= \frac{2V_{in}^2}{(A^2R'_{ac}+\frac{B^2}{R'_{ac}})^2}((2n_A^2k-2m_A^2\frac{1}{k^3})R'_{ac} \\ &\quad +(2n_B^2k-2m_B^2\frac{1}{k^3})/R'_{ac}) \end{aligned} \tag{15}$$

The system works at the CV operating frequency. Furthermore, the transfer parameter matrix of the leakage inductance model of the system is $B=0$, that is $m_B = n_Bk^2$.

$$\frac{\partial P_{out}}{\partial k} = \frac{2V_{in}^2}{(A^2R'_{ac}+\frac{B^2}{R'_{ac}})^2}(2n_A^2k-2m_A^2\frac{1}{k^3})R'_{ac} \tag{16}$$

Formula (16) is zero. The first derivatives of the left and right neighborhoods have opposite signs. The derivative of the system output power and output voltage to the coupling coefficient and the derivative of the coupling coefficient is zero at CV operating frequency. The system can resist offset at CV operating frequency. Similarly, the parameter $A=0$ in the transfer parameter matrix of the system leakage inductance model when the system works at the CC operating frequency, $m_A = n_Ak^2$, put this formula into formula (13)

$$\frac{\partial P_{out}}{\partial k} = \frac{2V_{in}^2}{(A^2R'_{ac}+\frac{B^2}{R'_{ac}})^2}((2n_B^2k-2m_B^2\frac{1}{k^3})/R'_{ac} \tag{17}$$

Formula (17) is zero, the first-order derivatives of the left and right neighborhoods have different signs, the output voltage to the coupling coefficient is zero, and the derivative of the output voltage to the coupling coefficient is zero. The system can resist offset under the CC operating frequency. Moreover, the parameter design method of the double-sided LCC compensation network that realizes CC/CV and ZPA under the determined coupling coefficient can be obtained. However, formula (18) is the double-sided LCC compensation network using the parameter design method CC4-CV3.

$$\begin{aligned} CC &\begin{cases} (X_3+\frac{X_1X_2}{X_1+X_2})(X_5+X_6)=X_4^2 \\ \frac{X_1X_2+X_1X_3+X_2X_2}{X_2^2} \\ \quad =\frac{X_5X_6+X_5X_7+X_6X_7}{X_6^2}=-\frac{1}{2} \end{cases} \\ CV &\begin{cases} (X_3+X_2)(X_5+X_6)=X_4^2 \\ \frac{X_1X_2+X_1X_3+X_2X_2}{X_2^2} \\ \quad =\frac{X_5X_6+X_5X_7+X_6X_7}{X_6^2}=-\frac{1}{2} \end{cases} \end{aligned} \tag{18}$$

E. PARAMETER DESIGN OF SYMMETRIC DOUBLE-SIDED LCC COMPENSATION NETWORK

The compensation network at the transmitting and receiving ends is the same. The transfer parameters AD of the leakage inductance model of the system are in the formula (19).

$$\begin{aligned} A &= \frac{X_1X_2+X_2X_3+X_1X_3}{X_2}\frac{X_2+X_3}{X_2}\frac{1}{X_4}-\frac{X_1+X_2}{X_2}\frac{1}{X_2}X_4 \\ D &= \frac{X_1X_2+X_2X_3+X_1X_3}{X_2}\frac{X_2+X_3}{X_2}\frac{1}{X_4}-\frac{X_1+X_2}{X_2}\frac{1}{X_2}X_4 \end{aligned} \tag{19}$$

It is not difficult to obtain from formula (19) when the transfer parameter of the leakage inductance model of the

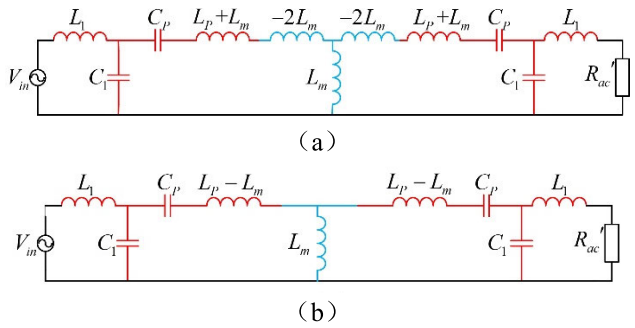

FIGURE 5. Cascaded equivalent T-type resonant network with CV output of double-sided LCC network.

system is $A = 0$. The system realizes CC output and ZPA. Therefore, the system realizes the ZPA at the CV operating frequency and can realize the CC/CV and ZPA. The system leakage inductance model's transfer parameters B, C are in formula (22).

$$B = (\frac{X_1X_2 + X_2X_3 + X_1X_3}{X_2})^2 \frac{1}{X_4} - (\frac{X_1 + X_2}{X_2})^2 X_4$$
$$C = \frac{1}{X_2^2} X_4 - (\frac{X_2 + X_3}{X_2})^2 \frac{1}{X_4} \quad (20)$$

From formula (20), the system achieves CV output, and there are four groups of formulas for ZPA, as shown in equations (21) (22) (23) (24).

$$X_2 + X_3 = X_4, X_1X_2 + X_2X_3 + X_1X_3 = (X_1 + X_2)X_4 \quad (21)$$
$$X_2 + X_3 = X_4, X_1X_2 + X_2X_3 + X_1X_3 = -(X_1 + X_2)X_4 \quad (22)$$
$$X_2 + X_3 = -X_4, X_1X_2 + X_2X_3 + X_1X_3 = -(X_1 + X_2)X_4 \quad (23)$$
$$X_2 + X_3 = -X_4, X_1X_2 + X_2X_3 + X_1X_3 = (X_1 + X_2)X_4 \quad (24)$$

Solving formula (21) can obtain $X_2^2 = 0$. Under the CV operating frequency, the reactance value of the parallel compensation capacitor is zero, which is not feasible. Solving formula (23) $b = 0$, which is not feasible. Therefore, the compensation network parameters satisfy equations (22) and (24), and the ZPA at the CV operating frequency can be realized. The parameters of the compensation network satisfy the formula (23), and the T-type two-port cascade equivalent of the system realizing CV output is shown in Figure 5(a). The parameters of the compensation network satisfy the formula (24), and the equivalent cascade of the T-type two-port network for the system to achieve CV output is in Figure 5(a).

Substitute the parameters of the compensation network into formulas (22) and (24) to obtain formulas (25) and (26).

$$\begin{cases} 2L_mL_1C_1C_P\omega_{cv}^4 - (L_m + L_P)C_P\omega_{cv}^2 + 1 = 0 \\ (L_P - L_m)C_1C_p\omega_{cv}^2 - (C_1 + C_P) = 0 \end{cases} \quad (25)$$

$$\begin{cases} 2L_mL_1C_1C_P\omega_{cv}^4 - (L_m - L_p)C_P\omega_{cv}^2 - 1 = 0 \\ (L_P + L_m)C_1C_p\omega_{cv}^2 - (C_1 + C_P) = 0 \end{cases} \quad (26)$$

The first formula in equations (25) and (26) realizes CV, and the second formula realizes CV and ZPA. For the IPT system, the coupling coefficient is determined. In order to calculate the compensation capacitor parameters, it is only necessary to determine the operating frequency and the compensation inductance. Substituting the calculated compensation capacitor parameters into formula (19). The transfer parameters can realize the CC and ZPA.

$$L_1C_1^2C_P^2(L_P^2 - L_m^2)\omega_{cc}^6 - L_1C_1C_PL_P(C_1 + C_P)\omega_{cc}^4 - C_1C_p^2(L_P^2 - L_m^2)\omega_{cc}^4 + (2C_1C_pL_1 + 2C_1C_pL_p + L_1C_P^2 + L_1C_1^2 + L_PC_P^2)\omega_{cc}^2 - (C_1 + C_p) = 0 \quad (27)$$

The CC/CV and ZPA parameter design method of the WPT system that realizes the symmetrical double-sided LCC compensation network can be obtained by giving the CV operating frequency and the compensation inductance ratio $A = D = 0$ in the formula (27).

III. THE EFFECT OF THE CAPACITANCE PARAMETER CHANGE

There is a deviation between the capacitance value configured in the practical and theoretical calculation values. The change of capacitance parameters will affect the current gain at the CC operating frequency. At CV operating frequency, it will affect the input phase angle characteristics of the system. The cascade equivalent of the CV of the T-type resonant network is shown in Figure 5(a). The double-sided LCC compensation network is equivalent to the cascade of three T-type resonant networks that realize CV-CV. The parameter matrix of the system is in the formula (28).

$$\begin{bmatrix} A_2 & jB_2 \\ jC_2 & D_2 \end{bmatrix} \begin{bmatrix} -1 & 0 \\ \frac{1}{jX_4} & -1 \end{bmatrix} \begin{bmatrix} D_2 & jB_2 \\ jC_2 & A_2 \end{bmatrix} \quad (28)$$

The expression of A_2, B_2, C_2 and D_2 shown in formula (29)

$$\begin{bmatrix} A_2 & jB_2 \\ jC_2 & D_2 \end{bmatrix} = \begin{bmatrix} \frac{X_1 + X_2}{X_2} & j\frac{X_1X_2 + X_1X_3 + X_2X_3}{X_2} \\ -j\frac{1}{X_2} & \frac{X_2 + X_3}{X_2} \end{bmatrix} \quad (29)$$

X_1 represents the reactance value of L_1 at CV operating frequency, X_2 the reactance value C_1 at CV operating frequency, and the series reactance value of C_P, L_P, L_m at CV frequency. According to formula (29), the CV output of the T-type resonant network can be realized when the parameter $B_2 = 0$. The resonance condition of the T-type resonant network is analyzed $B_1 = 0$, and we can get $A_2 = -X_1/X_3, D_2 = -X_3/X_1$. The voltage gain of the symmetrical double-sided LCC compensation network is consistently one under the CV operating frequency when the parameters of the compensation capacitor change.

A. THE EFFECT OF SERIES/PARALLEL COMPENSATION CAPACITANCE CHANGE ON THE SYSTEM

According to formula (29) $B_2 = 0$, the first T-type resonant network and the third T-type resonant network realize

CV-CV. According to formula (28), the second T-type resonant network can realize CV-CV at any frequency. Therefore, the double-sided LCC compensation network composed of three T-shaped resonant networks can realize the CV-CV. The formula (28) is expanded to obtain formula (30).

$$\begin{bmatrix} -A_2D_2 & 0 \\ -j\dfrac{1}{X_4}D_2^2 - 2jC_2D_2 & -A_2D_2 \end{bmatrix} \tag{30}$$

From the analysis of the resonant network $B = 0$, the output impedance of the T-type resonant network is:

$$Z_{in} = \frac{R_{ac} - jA_2C_2R_{ac}'^2}{D_2^2 + C_2^2R_{ac}'^2} \tag{31}$$

The transfer parameter matrix of the system after the cascaded resonant networks is consistent with the single resonant network. Under the CV operating frequency, the input phase angle of the WPT system of the double-sided LCC compensation network is determined by equation (32).

$$angle = \arctan(-\frac{1}{X_4}AD^3R_{ac}' - 2ACD^2R_{ac}') \tag{32}$$

The double-sided LCC network realizes CV, and the input phase angle characteristic is only related to the formula (33).

$$angle = \arctan(\frac{(X_2+X_3)^2(X_1+X_2)(-2X_4+X_2+X_3)R_{ac}}{X_4X_2^4}) \tag{33}$$

The input impedance angle will increase as the load resistance increases. The square term does not affect the capacitive and inductive phase angle of the double-sided LCC compensation topology input at the CV output since the X_4 is always positive.

$$(-2X_4 + X_2 + X_3)(X_1 + X_2) = (\omega L_1 - \omega\frac{1}{C_1})(-\omega L_m - \omega\frac{1}{C_1} - \omega\frac{1}{C_P} + \omega L_P) \tag{34}$$

According to the production standard requirements and regulations of the capacitor device, it is assumed that the actual compensation capacitance parameter floats between 0.9-1.1 times the theoretical capacitance parameter. The structural parameters of the double-sided LCC compensation network are shown in Table 2. The effect of series capacitance and parallel capacitance changes on the CV operating frequency is analyzed, and the influence of the input phase angle at the CV operating frequency is quantitatively analyzed.

The selection of CC and CV operating frequency of a double-sided LCC compensation network is described in detail in the paper [23] and will not be repeated here. Figure 6 shows the change of the series compensation capacitor to the CV operating frequency and the input impedance angle when the series compensation capacitor fluctuates in the range of 0.9-1.1 times the theoretically calculated value. The CV operating frequency decreases when the actual series compensation capacitor is larger than the theoretical calculation value. Figure 6(b) shows that the actual series compensation capacitance is smaller than the theoretical calculation value, and the input impedance angle of the double-sided LCC compensation network at the CV operating frequency is inductive. Figure 7 shows the CV operating frequency and input impedance angle change when the parallel compensation capacitor changes in the range of 0.9-1.1 times the theoretically calculated value. The actual parallel capacitance is larger than the theoretical calculation value, and the CV operating frequency decreases; the parallel capacitance is smaller than the theoretical calculation value, and the CV operating frequency increases. With the increase of the actual parallel compensation capacitance, the input impedance angle of the double-sided LCC compensation network at the CV operating frequency is inductive. The practical parallel compensation capacitor is too large; the series compensation capacitor is too small, and the system is inductive. The practical parallel compensation capacitor is too small, and the system is capacitive.

Figure 8 shows that the series compensation capacitance is larger than the theoretical calculation value, and the CC

TABLE 2. Parameters of double-sided LCC compensation network.

Parameters	Value	Parameters	Value
Self-inductance of Transmitter Coil	120μH	Self-inductance of receiver coil	120μH
Coupling coefficient	0.1625	Compensation inductance ratio	0.375
Primary compensation inductance	45μH	Secondary compensation inductance	45μH
The primary series compensation capacitor	117.085nF	The secondary series compensation capacitor	117.085nF
The primary parallel compensation capacitor	42.379nF	The secondary parallel compensation capacitor	42.379nF

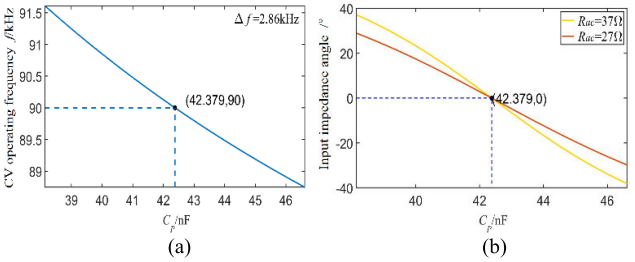

FIGURE 6. (a) Series compensation capacitance influence on CV frequency (b) Series compensation capacitance influences on input impedance angle.

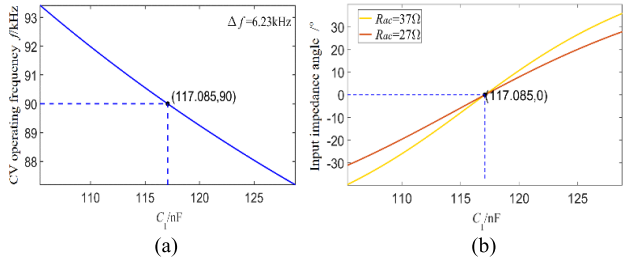

FIGURE 7. (a) Parallel compensation capacitance influence on CV frequency (b) Parallel compensation capacitance influence on input impedance angle.

TABLE 3. Parametric design method analysis.

Resonance Condition	Restrictions	Parametric Design Equations	Frequency Characteristic Curve of Transfer Parameters
$CC2-CV3$	$\omega_{cc}, \xi_1, \xi_2$.	$(a-\frac{1}{a}-\frac{k^2(\xi_2-b)}{ab^2})(a-\frac{1}{a})=a^2k^2$ $\frac{a^2k^2}{\xi_1}+\frac{(a-\frac{1}{a})(a\xi_2-\frac{b}{a})}{b^2}=\frac{1}{a^2}$ $b=1/(\omega_{cc}{}^2L_PC_2)$ $a=\sqrt{\frac{\sqrt{\xi_1}}{k}}$ $b=\xi_2a^2$	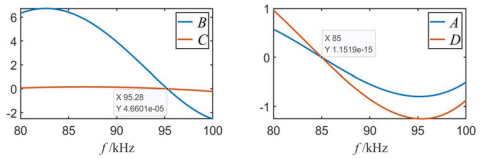
$CC2-CV1$	$\omega_{cc}, \xi_1, \xi_2$.	$a^2-\frac{k^2(\xi_2-b)}{b^2}=1+\frac{k^2a^4}{a^2-1}$ $b=1/(\omega_{cc}{}^2L_PC_2)$ $(\frac{\sqrt{\xi_1}}{k}-1)^2(1+\frac{k^4}{\xi_1\xi_2})=\xi_1$	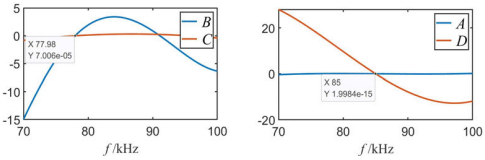
$CC4-CV1$	$\omega_{CV}, \xi_1, \xi_2$.	$(a-\frac{1}{a}-\frac{\xi_1b}{a(b-\xi_1)}-\frac{\xi_1b}{a\xi_1-b/a})(a-\frac{1}{a}+\frac{k^2(\xi_1-b)}{ab^2})=a^2k^2$ $(a-\frac{1}{a}+\frac{k^2(\xi_1-b)}{ab^2}+\frac{\xi_2}{a}-\frac{\xi_2^2}{a\xi_2-\xi_2/a})(a-\frac{1}{a}-\frac{\xi_1b}{a(b-\xi_1)}-\frac{b}{a})=a^2k^2$ $b=1/(\omega_{cv}{}^2L_PC_2)$	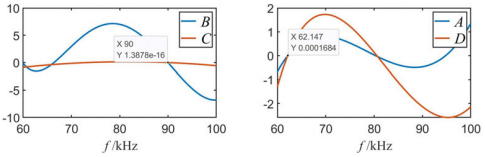
$CC1-CV3$	$\omega_{cc}, \xi_1, \xi_2$.	$b^4(b^2-1)^2-b^4k^2(b^2-1)^2-2b^2(b^2-1)^2$ $-(\xi_1+\xi_2)(b^2-1)^2+\xi_1\xi_2=0$ $(b^2k-1-b^2)(b^2k-1+b^2)=0$ $\frac{1}{\xi_1}+\frac{1}{\xi_2}=\frac{(1\pm k)^2}{k^2}$	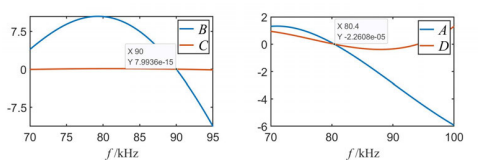

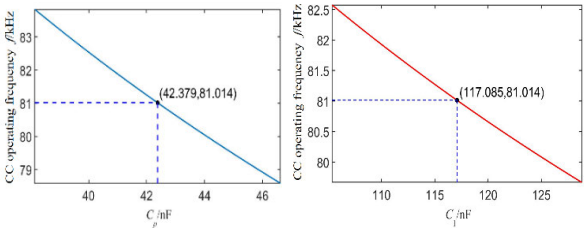

FIGURE 8. (a)Series compensation capacitance influence on CC frequency (b)Parallel compensation capacitance influence on CC frequency.

working frequency is reduced. Considering the stability of current gain and parasitic resistance, the criterion of load stability of CC operating frequency is that the CC operating frequency of the selected system decrease. The series compensation capacitance is smaller than the theoretical value, and the CC operating frequency selected by the constant current operating frequency selection criterion increase. As the theoretical calculation value of the parallel compensation capacitance ratio increases, the CC operating frequency selected by the CC operating frequency decreases. As the series compensation capacitance is smaller than the theoretical value, the CC operating frequency selected by the CC operating frequency criterion increases.

B. INFLUENCE OF COMPENSATION CAPACITANCE CHANGE ON SYSTEM AND IMPLEMENTATION OF SAEJ2954 STANDARD

By adjusting the parameters of the compensation capacitor, the operating frequency can meet the SAEJ2954 standard. This paper defines the ratio of the actual series compensation capacitor to the theoretical calculation value as $a(0.9 \leq a \leq 1.1)$; the ratio of the actual parallel compensation capacitor to the theoretical calculation value $b(0.9 \leq b \leq 1.1)$. Figures 6(a) and 7(a) show that the sensitivity of CV working frequency to parallel compensation capacitor is greater than that of CV working frequency to series compensation capacitor. Figure 8 shows that the CC working frequency is susceptible to the parallel compensation capacitor. Therefore, the practical parallel compensation capacitance is greater than the theoretical calculation value, while the actual series compensation capacitance is less than the theoretical calculation value. The CV working frequency and CC working frequency of the system can meet the standard SAEJ2954. With the change of compensation capacitance, the projection of CC working frequency on the X-Y plane is in Figure 9(a). The standard that meets SAEJ2954 is yellow, and the standard that does not meet is blue. With the change of compensation capacitance, the projection of CV working frequency on the X-Y plane is in Figure 9(b). Combined with Figure 9, the value of a series

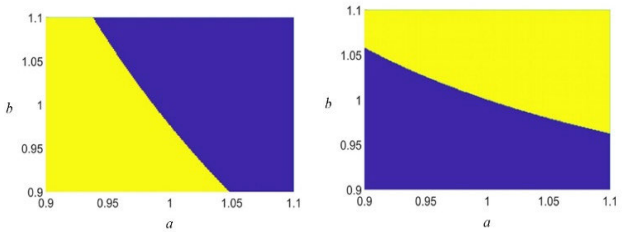

FIGURE 9. (a)Compensation capacitance variation influence on CC frequency (b)Compensation capacitance variation influence on CV frequency.

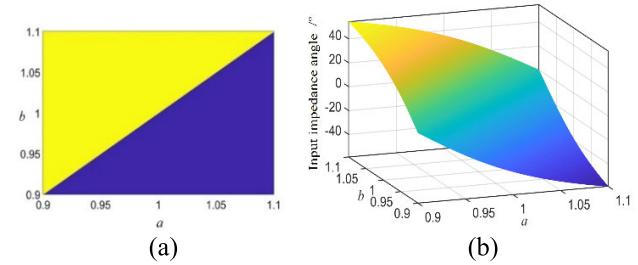

FIGURE 10. Compensation capacitance variation influences the input phase angle of the system.

compensation capacitor or parallel compensation capacitor meeting the SAEJ2954 standard can be obtained. And the change of input impedance angle of a double-sided LCC compensation network in Figure 9.

The system is inductive and defined as 1; the system is capacitive and defined as -1; the system realizes ZPA and is defined as 0. Figure 10 is the diagram of the influence of compensation capacitance change on the input phase angle characteristics of the system. The yellow part indicates that the input phase angle characteristic of the system is inductive at CV operating frequency; The blue part indicates capacitive. The intersection between blue and yellow indicates the ZPA. The ratio of the parallel compensation capacitance to the theoretical calculation value is smaller than the series compensation capacitance, and the input phase angle characteristic of the system is capacitive. Furthermore, the system must be inductive when the ratio of parallel compensation capacitance to theoretical calculation value is greater than that in series. With the increase of the parallel compensation capacitance and the theoretical calculation value or the decrease of the series compensation capacitance and the theoretical calculation value, the capacitive angle of the input phase angle of the system is more significant.

C. REALIZATION OF ZVS AT CC OR CV WORKING MODE

In practice, the inverter's output current is the system's input current, and there are many higher-order harmonic components whose phase lags behind the fundamental wave. At this time, only the fundamental wave analysis method is used to analyze the error. Therefore, it is necessary to analyze whether the input current of the system still meets the zero phase angle characteristic or whether ZVS can be opened when considering the high harmonic current. In this paper,

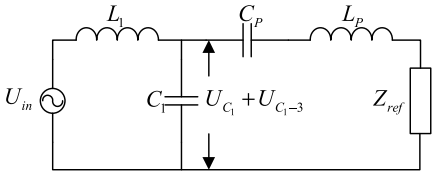

FIGURE 11. Simplified model of the system considering the third harmonic.

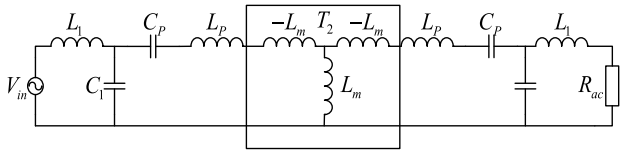

FIGURE 12. Equivalent of T-type resonant network based on leakage inductance model.

the impedance of the receiving end under higher harmonics is converted to the transmitting end, and the system is equivalent to the simplified model, as shown in Figure 11. The ratio of higher harmonic voltage to fundamental voltage at both ends of the parallel compensation capacitor at the transmitter is analyzed. It is found that after the higher harmonics are greater than three times, the voltage at both ends of the parallel compensation capacitor at the transmitting end can be ignored [24]. Through the superposition theorem, the fundamental wave voltage of the input square wave, the fundamental wave voltage at both ends of the capacitor, and the third harmonic voltage are superimposed. Calculate the current flowing through the compensation inductance at the transmitter. Figure 11, U_{in} represents the square wave with dead band of the input system, U_{C_1} and U_{C_1-3} represent the fundamental voltage and the third harmonic voltage of the parallel compensation capacitor at the transmitter, respectively, and Z_{ref} represents the value of the impedance at the receiver converted to the transmitter.

First, the feasibility of this simplified system model considering higher harmonics is analyzed, and the impedance of the receiving end converted to the value of the transmitting end under higher harmonics is analyzed. In order to facilitate the analysis, the leakage inductance model of the IPT system of the double-sided LCC compensation network is divided into three equivalent T-type resonant networks, as shown in Figure 12.

The T-parameter matrix of the T-type resonant network of T_2 is shown in formula (35). According to the literature [25], the ratio of the AC equivalent resistance at the receiving end to the series compensation inductance at the receiving end is relatively small, but its modeling is relatively complex. Therefore, to facilitate analysis, the AC equivalent resistance R_{ac} at the fundamental wave is used to replace the AC equivalent resistance at the higher harmonic.

$$T_2 = \begin{bmatrix} 0 & -j\omega L_m \\ \frac{1}{j\omega L_m} & 0 \end{bmatrix} \tag{35}$$

Let the load impedance of the T-type resonant network T_2 be Z, and the input impedance of T_2 is $\omega^2 L_m^2/Z$ according to formula (34). Moreover, the higher harmonic model of the

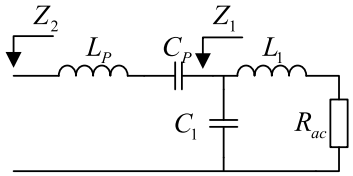

FIGURE 13. T resonant network at the receiving end with high order harmonics.

receiver is analyzed, and the T-type resonant network of the receiver is shown in Figure 13. It is very complicated to model the AC equivalent resistance under the high order harmonics; Therefore, to simplify the analysis, the AC equivalent load under the fundamental wave is used to replace the AC equivalent load under the higher harmonics. The actual AC equivalent load under the higher harmonics is minimal.

Assuming that the operating frequency of the system is ω and the harmonic number is n, the expression of impedance Z_1 at the receiving end is formula (36) and the expression of impedance Z_2 is formula (37) under n-th harmonics

$$Z_1 = \frac{(jn\omega L_1 + R_{ac})(-j\frac{1}{n\omega C_1})}{jn\omega L_1 - j\frac{1}{n\omega C_1} + R_{ac}} \tag{36}$$

$$Z_2 = jn\omega_{cc}L_P - j\frac{1}{n\omega_{cc}C_P} + Z_1 \tag{37}$$

Substitute Equation (36) into Equation (37) to get, as in (38), shown at the bottom of the next page.

Taking the compensation network parameters in Table 2 as an example, the angle of the input impedance angle Z at the receiving end under the nth harmonic is shown in Figure 14. The figure only lists the impedance angle from the third harmonic to the eleventh harmonic because the input impedance angle of the receiver is almost equal to 90° as the number of harmonics increases.

Under higher harmonics, the real part of Z_2 is tiny compared with the imaginary part. Under the parameters designed in this paper, the ratio between the imaginary part and the real part of the receiver is about 749 under the third harmonic, so the real part can be ignored. The input impedance angle at the receiving end will only be larger when the AC resistance at the high-order harmonic is used. Therefore, under the high-order harmonic, the influence of the AC equivalent resistance of the system on the high-order harmonic modeling at the transmitting end can be ignored. In the same way, it is easy to know that $j(n\omega L_1 - 1/n\omega C_1)/n^2\omega^2 C_1^2\left[R_{ac}^2 + (n\omega L_1 - 1/n\omega C_1)^2\right]$ in formula (38) can also be ignored under higher harmonics. Under the third harmonic, the ratio of neglected impedance to total impedance is about 0.0023; Therefore, the impedance of the receiving end can be expressed by equation (39).

$$Z_2 \approx jn\omega L_P - j\frac{1}{n\omega C_P} - j\frac{1}{n\omega C_1} \tag{39}$$

Figure 15 shows the curve of the ratio of the difference between the approximate equivalent value and the actual value of Z_2 and the actual value ΔZ_2 with the load under the third harmonic.

According to Figure 15, under the third harmonic, when the equivalent load resistance is 10Ω, the maximum error is about 1.9%. Take the impedance of the receiving end into formula (35), and the impedance Z_3 of the receiving end converted to the transmitting end under higher harmonics is shown in formula (40). And the T-type resonant network at the transmitter is shown in Figure 16.

$$Z_3 = -j\frac{n^4\omega^4 C_P C_1 L_m^2}{n^3\omega^3 L_P C_p C_1 - n\omega C_P - n\omega C_1} \tag{40}$$

As can be seen from Figure 16, the expression of Z_4 is shown in Formula (41)

$$Z_4 = -j\frac{1}{n\omega C_1} - \frac{1}{n^2\omega^2 C_1^2\left(jn\omega L_p - j\frac{1}{n\omega C_p} - j\frac{1}{n\omega C_1} - Z_3\right)} \tag{41}$$

Similar to the previous analysis, the second term in equation (41) is negligible under higher harmonics, so $Z_4 \approx -j/n\omega C_1$. Under higher harmonics, the receiver compensation inductance and equivalent AC load can be ignored when converted to the transmitter. Therefore, when the load or the receiver compensation inductance changes, the impact on the impedance conversion value can be ignored. The simplified model of the system under higher harmonics is shown in Figure 17.

In the figure, V_{in-n} represents the n-th harmonic component of the square wave with dead band in Fourier series expansion of the system input, and U_{C_1-n} represents the voltage on both sides of the parallel compensation capacitor at the transmitter under the n-th harmonic. It is not difficult to see from Figure 17 that the high-order harmonic component of the compensation inductance at the transmitting end lags the fundamental current by 90 °, and the expression of V_{in-n}, U_{C_1-n} is shown in Formula (42) (43). And $n = 1, 3, 5 \ldots 2m+1$.

$$V_{in-n} = \frac{4V_{DC}}{\pi}\frac{\sin n\omega t \sin\frac{\pi nk}{2}}{n} \tag{42}$$

$$U_{C_1-n} = \frac{4V_{DC}}{\pi}\frac{\sin n\omega t \sin\frac{\pi nk}{2}}{n}\frac{-\frac{1}{n\omega C_1}}{jn\omega L_1 - \frac{1}{n\omega C_1}} \tag{43}$$

k represents the duty cycle of the square wave, V_{DC} represents the input DC voltage of the inverter, and defines the ratio of the voltage U under the higher harmonics at the two ends of the parallel compensation capacitor C_1 at the transmitter end to the fundamental voltage U_{C_1-n} at the two ends of U_{C_1} as δ_n

$$\delta_n = \frac{U_{C_1-n}}{U_{C_1}} \tag{44}$$

Under the constant current/constant voltage operating frequency, as long as the voltage at both ends of C_1 under different higher harmonics is compared with the voltage at C_1 under the fundamental wave, it can be concluded that the parallel compensation capacitance is small enough to ignore the number of harmonics above. At this time, the simplified model of the system is shown in Figure 18 when considering higher harmonics.

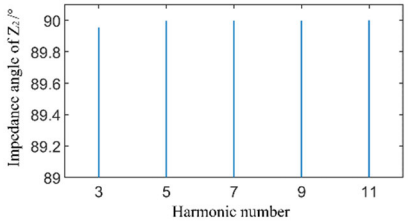

FIGURE 14. Input impedance angle of receiver end with N-th harmonic.

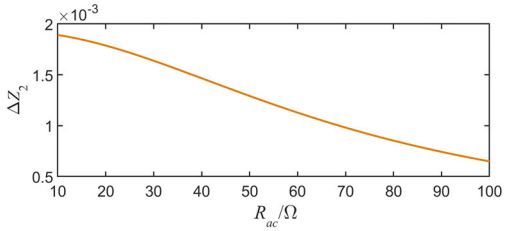

FIGURE 15. Load variation curve of impedance error value at the receiving end with the third harmonic.

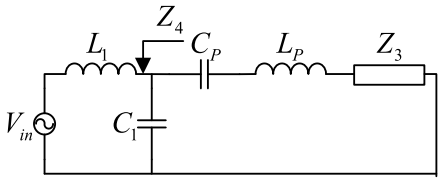

FIGURE 16. T resonant network at the transmitting end after impedance conversion at the receiving end.

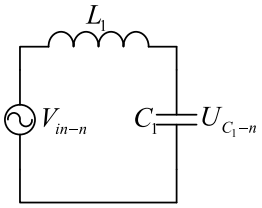

FIGURE 17. Simplified model of system considering third-order harmonic.

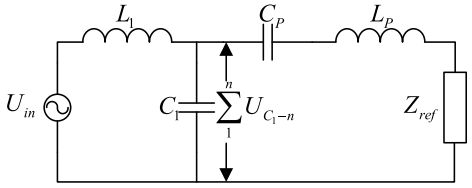

FIGURE 18. Simplified model of system considering third-order harmonic.

In the time domain, the current flowing through the transmitting end compensation inductor can be obtained by integrating the voltage at both ends of the transmitting end compensation inductor. That is, the inverter's output current

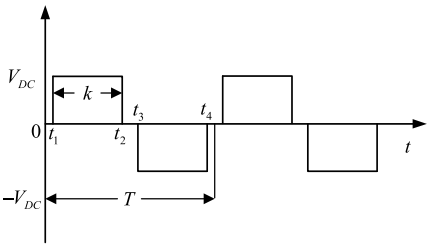

FIGURE 19. Diagram of input voltage.

is as shown in formula (45).

$$I_{IN}(t) = \frac{\int_0^T [U_{in}(t)]dt - \int_0^T [U_{C_1}(t)]dt - \sum_3^n \int_0^T [U_{C_1-n}(t)]dt}{\omega L_1} \tag{45}$$

In the formula, the input square wave $U_{in}(t)$ with dead time is a piecewise function, which requires piecewise integration and initial value calculation; The voltage $U_{C_1}(t)$ and $U_{C_1-n}(t)$ at both ends of the parallel compensation capacitor at the transmitter under the fundamental and higher harmonics are trigonometric functions with $T = 2\pi/n\omega$ as the period, so $U_{C_1}(t)$ and $U_{C_1-n}(t)$ can be directly integrated. First, integrate $U_{in}(t)$, define the current after $U_{in}(t)$ integration as $I_0(t)$, and input the square wave with dead time, as shown in Figure 19. In the figure k represents the duty cycle of the square wave and V_{DC} represents the input DC voltage of the inverter.

In the Figure19, $t_1 = (1-k)\pi/2\omega$, $t_2 = (1+k)\pi/2\omega$, $t_3 = (3-k)\pi/2\omega$, $t_4 = (3+k)\pi/2\omega$. According to Figure 19, the current expression after integration is shown in Formula (46).

$$\begin{cases} I_0(t) = I_0(0) & 0 < t < t_1 \\ I_0(t) = V_{DC}(\omega t - \dfrac{(1-k)\pi}{2}) + I_0(0) & t_1 < t < t_2 \\ I_0(t) = V_{DC}k\pi + I_0(0) & t_2 < t < t_3 \\ I_0(t) = -V_{DC}(\omega t - \dfrac{(3+k)\pi}{2}) + I_0(0) & t_3 < t < t_4 \\ I_0(t) = I_0(0) & t_4 < t < T \end{cases} \tag{46}$$

$I_0(t)$ is a function with a period of T, then $I_0(t = \pi/\omega) = -I_0$. Substitute its condition into equation (45) to obtain the initial value $I_0(t)$ of $I_0(0)$, as shown in equation (47).

$$I_0(0) = -\frac{V_{DC}k\pi}{2} \tag{47}$$

Under different operating frequencies, the reactance value of the compensation network in the compensation network is different, resulting in the change of the transmission parameter matrix of the system. Under the fundamental wave, the phase angle characteristics of the input ports of the system

$$Z_2 = jn\omega L_P - j\frac{1}{n\omega C_P} - j\frac{1}{n\omega C_1} - \frac{-R_{ac} + j(n\omega L_1 - \frac{1}{n\omega C_1})}{n^2\omega^2 C_1^2\left[R_{ac}^2 + (n\omega L_1 - \frac{1}{n\omega C_1})^2\right]} \tag{38}$$

are different. Therefore, for the voltage $U_{C_1}(t)$ and $U_{C_1-n}(t)$ at both ends of the transmitting end compensation capacitor under the fundamental wave, it is necessary to aim at different operating frequencies. Considering the phase angle characteristics of the fundamental wave at different operating frequencies, The voltage at both ends of the transmitter compensation capacitor is modeled to analyze whether the system me at different operating frequencies.

1) ZVS OF CC WORKING MODE

In the T parameter matrix of the system, the parameter A is 0, and the CC and ZPA is realized. The parameters BC of the system are in the formula (48).

$$(X_1 + X_2)\,X_4^2 - (X_2 + X_3)(X_1X_2 + X_1X_3 + X_2X_3) = 0 \tag{48}$$

$$B = (\frac{X_1X_2+X_2X_3+X_1X_3}{X_2})^2 \frac{1}{X_4} - (\frac{X_1+X_2}{X_2})^2 X_4$$
$$C = \frac{1}{X_2^2}X_4 - (\frac{X_2+X_3}{X_2})^2 \frac{1}{X_4} \tag{49}$$

The CC operating frequency of the system is ω_{cc}, the input current of the system under the fundamental wave is, as in (50), shown at the bottom of the next page.

The voltage across the parallel compensation capacitor at the transmitting under the fundamental wave is

$$U_{C_1} = 4\frac{V_{DC}}{\pi}\sin\frac{\pi}{2}k - jI_{in}\omega_{cc}L_1 \tag{51}$$

Substitute the compensation network parameters in TAB 2, and the square wave ratio of the output in the inverter is 0.98. The current of the LC compensation network at the transmitter end is modeled. It is necessary to consider the voltage of the parallel compensation capacitor at the transmitting end under the third harmonic. The output current of the inverter at the CC operating frequency is calculated as follows:

$$\omega_{cc}L_1I_{IN}(t) = I_0(t) - \int_0^T [U_{C_1}(t) + U_{C_1-3}(t)]dt \tag{52}$$

The voltage across the parallel compensation capacitor at the transmitting end and the time domain expression under the third harmonic are as follows:

$$\begin{aligned} U_{C_1-3}(t) &= \frac{4V_{DC}\sin\frac{\pi nk}{2}}{n\pi}\sin\left(n\omega_{cc}t - \frac{\pi}{2}\right) \\ &\quad\times\left|\frac{1}{(-9\omega_{cc}^2L_1C_1+1)}\right| \\ U_{C_1}(t) &= 4\frac{V_{DC}}{\pi}\sin\frac{\pi}{2}k\sin\omega_{cc}t + I_{in}\omega_{cc}L_1 \\ &\quad\times\left(\sin\omega_{cc}t - \frac{\pi}{2}\right) \end{aligned} \tag{53}$$

Integrate the tertiary voltage and the fundamental voltage across the parallel compensation capacitor at the transmitting end to obtain the formula

$$\int_0^T U_{C_1-3}(t) = \frac{-4V_{DC}\sin\frac{3\pi k}{2}}{3\pi}\sin 3\omega_{cc}t\left|\frac{1}{(-9\omega_{cc}^2L_1C_1+1)}\right|$$

$$\int_0^T U_{C_1}(t) = \frac{-4V_{DC}}{\pi}\sin\frac{\pi}{2}k\cos\omega_{cc}t - I_{in}\omega_{cc}L_1\sin\omega_{cc}t \tag{54}$$

Substitute the design parameters in TAB 2 into the system, the input current theoretically/simulation values under the CC operating frequency in Figure 20.

The absolute value of the theoretically calculated value is slightly larger than the simulated value at the end of the dead zone. The influence of parasitic resistance is considered during the simulation, and the input impedance of the system during the simulation is smaller than the input impedance during the theoretical calculation, resulting in the simulated value of the input current under the fundamental wave being more significant than the theoretically calculated value and all positive. The system load is 35Ω, and the error is 3.16%. As the load decreases, the deviation will become smaller. The system load is 15Ω, and the deviation is 0.5%. The drain-source voltage of the MOSFET drops to the on-state voltage drop at the turn-on, and the system's input current is less than zero to achieve ZVS. Therefore, for the system input current of the double-sided LCC compensation network, the input current $I_{IN}(t_1) < 0$ and $I_{IN}(t_3) > 0$ can realize the ZVS of the MOSFET. Due to the symmetry of the input current of the double-sided LCC compensation network, $I_{IN}(t_1) < 0$ is required to achieve ZVS. Figure 11 shows $I_{IN}(t_1) < 0$, the symmetrical double-sided LCC compensation network can realize ZVS under the CC operating frequency.

2) ZVS OF CV WORKING MODE

The system works at the CC operating frequency under the fundamental wave and realizes the input ZPA. After considering the high-order harmonic components of the input current, the inverter can realize ZVS. The ratio b between the series compensation capacitor and the theoretical calculation value is greater than the ratio a between the parallel compensation capacitor and the theoretical calculation value. The input impedance of the system is inductive under the fundamental wave, and the symmetrical double-sided LCC compensation network can realize ZVS after considering high-order harmonic. Modeling the input current of the system under the CC operating frequency, the high-order harmonic components of the input current lag the fundamental current by 90°, so the input phase angle is weak capacitive under the fundamental wave. This section quantitatively gives the range of variation of the ZVS of the inverter switch tube that the compensation capacitor can achieve. The modeling method for the system input current at the CV operating frequency is similar to the CC operating frequency.

$$\begin{aligned} I_{IN}(t) &= I_{in}\sin\omega_{cv}(t-\varphi) + \frac{I_0(t)}{\omega_{cv}L_1} \\ &\quad + \frac{4V_{DC}}{\pi\omega_{cv}L_1}\sin\frac{\pi}{2}k\cos\omega_{cv}t \\ &\quad + \frac{4V_{DC}\sin\frac{3\pi k}{2}}{3\pi\omega_{cv}L_1}\sin 3\omega_{cv}t\left|\frac{1}{(-9\omega_{cv}^2L_1C_1+1)}\right| \end{aligned} \tag{55}$$

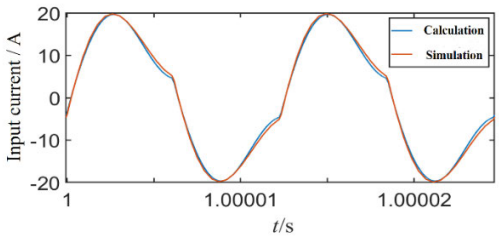

FIGURE 20. Input current of the system at CC frequency.

$I_{in}\sin\omega_{cv}(t-\varphi)$ is the fundamental wave of the input current in system. The relationship between the input and output voltage/current under the fundamental wave is in formula (56).

$$\begin{cases}\dot{V}_{in} = -AD\dot{V}_{out} \\ \dot{I}_{in} = (-j\frac{1}{X_4}D^2 - 2jCD)\dot{V}_{out} - AD\dot{I}_{out}\end{cases} \tag{56}$$

The double-sided LCC compensation network has the same compensation network, the parameter $AD = 1$, the input current under the fundamental wave is, as in (57), shown at the bottom of the next page.

The formula's input current is the system's fundamental current component $I_{in}\sin\omega_{cv}(t-\varphi)$ (58).

$$\begin{aligned}&\mathrm{I_{in}sin\omega_{cv}\,(t-\varphi)} \\ &\quad=\frac{\mathrm{V_{in}sin\omega_{cv}t}}{\mathrm{R_{ac}}} \\ &\qquad+\frac{(\omega_{cv}^2\mathrm{L_P}+\omega_{cv}^2\mathrm{L_m}-\frac{1}{\mathrm{C_1}}-\frac{1}{\mathrm{C_P}})}{\mathrm{L_m}\frac{1}{\mathrm{C_1^2}}} \\ &\qquad\cdot(\omega_{cv}^2\mathrm{L_P}-\omega_{cv}^2\mathrm{L_m}-\frac{1}{\mathrm{C_1}}-\frac{1}{\mathrm{C_P}})\mathrm{V_{in}cos\omega_{cv}t}\end{aligned} \tag{58}$$

The actual parallel compensation capacitance is 114.4nF, and the ratio to the theoretical calculation value is about 0.9771; the actual series compensation capacitance is 42.8nF, and the ratio to the theoretical calculation value is about 1.012. According to the above analysis, the input impedance of the system is capacitive under the fundamental wave. Bring the parameters of the compensation capacitor into the formula (42) to obtain the CV operating frequency and the input current of the system in Figure 21.

However, the system's load varies at the CV operating frequency, and it is more complicated to model the input current under each load. For the switch tube of the inverter, ZVS can be realized only by inputting the current $I_{IN}(t_1) < 0$ at the end of the dead time. Therefore, it is only necessary to calculate the input current at the end of the dead zone. The positive half-cycle of the voltage is the current at the end of the dead zone in formula (59), as shown at the bottom of the next page.

TABLE 4. Compensation parameters.

Compensation parameters			
L_1	45μH	C_S	42.8nF
L_2	45μH	C_1	114.4nF
C_P	42.8nF	C_2	114.4nF

As the load changes, it only $V_{in}\sin\omega_{cv}t_1/R_{ac}$ changes. And as the load increases, $V_{in}\sin\omega_{cv}t_1/R_{ac}$ decreases. Therefore, $I_{IN}(t_1) < 0$ achieved at the maximum load within the load range, all loads within the load range can make the inverter switch Tubes implement ZVS. When the load range is $35 \sim 55\Omega$, the DC load is 55Ω, and the compensation capacitor changes by $0.9 \sim 1.1$ times, the current value when the switch is turned on in Figure 13. Define the ratio of the actual series compensation capacitance to the theoretically calculated value as $a(0.9 \le a \le 1.1)$ and the ratio of the actual parallel compensation capacitance to the theoretically calculated value as $b(0.9 \le b \le 1.1)$.

The yellow part in the figure represents the variation range of the compensation capacitance that enables the switch to achieve the ZVS, and the blue is the variation range of the compensation capacitor that cannot enable the switch to achieve the ZVS. It can be obtained from Figure 23 that when the input impedance of the system under the fundamental wave is capacitive, the compensation capacitor can make the switch tube realize the allowable variation range of the ZVS.

IV. EXPERIMENTAL VERIFICATION

The experiment of the WPT system is in Figure 24. The power supply is Chroma 62150h-600s, which is the input voltage of the WPT system. The electronic load is Chroma-63804. The FPGA generates the complementary PWM drive with a dead zone, and the full-bridge inverter is controlled by an optocoupler and drive chip. CREE C3M0065090 with a small trailing current is selected for the inverter, and the drive chip uses the MOSFET driver 2EDL23N06PJ produced by Infineon. This paper designed two groups of experiments to verify that the inverter realizes ZVS when the input impedance angle of the system is inductive and capacitive, respectively. The input voltage is 200V, and the compensation network parameters are in Table 4 and Table 5. The double-sided LCC compensation network has three constant current operating frequency points and four constant voltage operating frequency points. The author's paper analyzed how to select appropriate CC/CV operating frequency points [23], so this paper will not repeat it.

The input voltage is 200V, and the input phase angle of the system is capacitive under the CV working frequency. The CC working frequency of the system is 81.169 kHz, and the CV working frequency is 90.580 kHz. The current gain,

$$I_{in} = \frac{\omega_{cc}^3 L_p C_1 C_P R_{ac} V_{in}}{\omega_{cc}^3 L_1 C_1 C_p - \omega_{cc} C_p + \omega_{cc}^2 L_1 C_P + \omega_{cc}^2 L_P C_P + \omega_{cc}^2 L_1 C_1 - 1 - \omega_{cc}^4 L_1 L_P C_1 C_p} \tag{50}$$

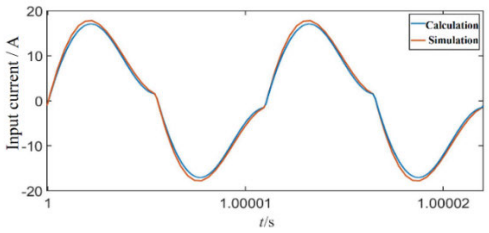

FIGURE 21. Input current of the system at CV frequency.

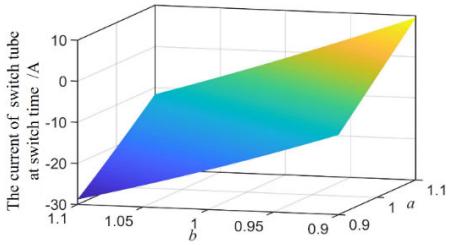

FIGURE 22. Influence of the change of compensation capacitance on the current at the opening time of the switch.

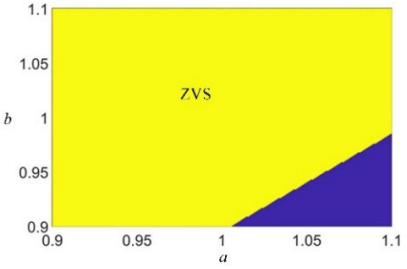

FIGURE 23. Influence of compensation capacitance on ZVS of the switch.

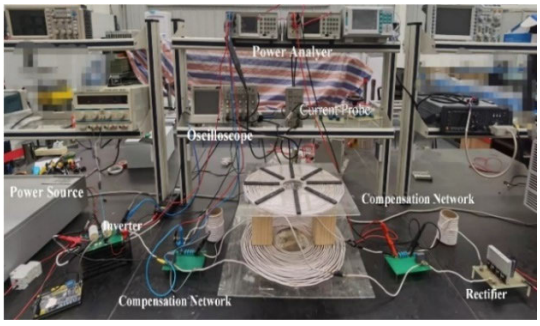

FIGURE 24. WPT system experimental platform.

voltage gain, and input-phase angle under CC/CV operating frequency are in Figure 16.

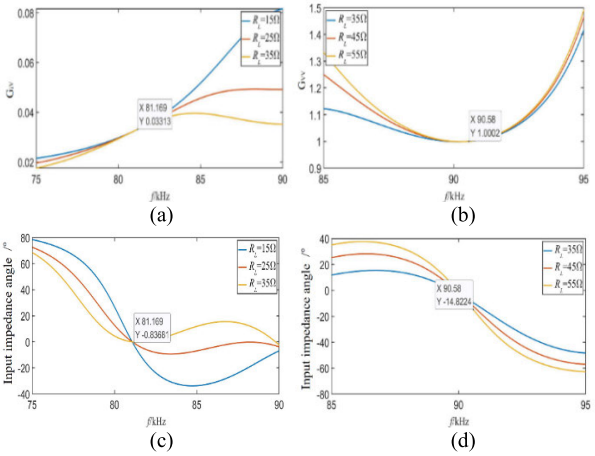

FIGURE 25. Output characteristics of the WPT system (a)current gain (b)voltage gain (c)input impedance angle at the CC frequency (d)input impedance angle at CV frequency.

TABLE 5. Compensation parameters.

Compensation parameters			
L_1	45μH	C_S	39.8nF
L_2	45μH	C_1	121nF
C_P	39.8nF	C_2	121nF

Figure 25(a) shows that the current gain of the system is almost unchanged with the load change. The system can realize CC output under different loads of CC working frequency. Figure 25(b) shows that the voltage gain of the system is almost constant with the load change. The system can achieve CV output under different loads at CV working frequency. It is not difficult to see from figure 25(c) that the input impedance angle of the system almost reaches ZPA under CC working frequency and different loads. Figure 25(d) shows that the input impedance angle of the system is capacitive under CV operating frequency and different loads. The output power is 1kW, the maximum capacitance angle of the input impedance of the system is about, and the inverter realizes ZVS.

The input voltage of the second set of experiments is 100V, and the parameters of compensation inductance and capacitance are in Table 5. The CC operating frequency of the system is 82.24kHz, and the CV working frequency is 89.93kHz. The operating frequencies of CC and CV are

$$\frac{\dot{V}_{in}}{R_{ac}}+j\frac{(\omega_{cv}^2L_P+\omega_{cv}^2L_m-\frac{1}{C_1}-\frac{1}{C_P})(\omega_{cv}^2L_P-\omega_{cv}^2L_m-\frac{1}{C_1}-\frac{1}{C_P})\dot{V}_{in}}{L_m\frac{1}{C_1^2}} \tag{57}$$

$$I_{IN}(t_1)=\frac{I_0(t_1)}{\omega_{cv}L_1}+\frac{4V_{DC}\sin\frac{\pi}{2}k\cos\omega_{cv}t_1}{\pi\omega_{cv}L_1}+\frac{4V_{DC}\sin\frac{3\pi k}{2}\sin3\omega_{cv}t_1}{3\pi\omega_{cv}L_1\left|-9\omega_{cv}^2L_1C_1+1\right|}+\frac{V_{in}\sin\omega_{cv}t_1}{R_{ac}}$$
$$+\frac{(\omega_{cv}^2L_P+\omega_{cv}^2L_m-\frac{1}{C_1}-\frac{1}{C_P})(\omega_{cv}^2L_P-\omega_{cv}^2L_m-\frac{1}{C_1}-\frac{1}{C_P})}{L_m\frac{1}{C_1^2}}V_{in}\cos\omega_{cv}t_1 \tag{59}$$

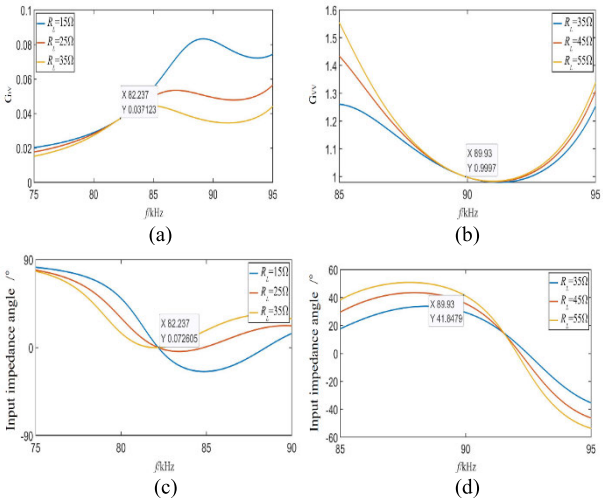

FIGURE 26. Output characteristics of the WPT system (a)current gain (b)voltage gain (c)input impedance angle at the CC frequency (d)input impedance angle at CV frequency.

within the SAEJ2954 standard. The current gain, voltage gain, and input-phase angle under CC/CV operating frequency are in Figure 17.

From figure 25(a)/26(a), with the change of load, the current gain of the system is almost unchanged. The system can achieve CC output under different loads at the CC operating frequency. From figure 25(a)/26(b), with the change of load, the voltage gain of the system is almost unchanged. The system can achieve CV output under different loads at the CV operating frequency. It can be seen from figure 25(c)/26(c) that under the CC operating frequency and different loads, the input impedance angle of the system almost achieves ZPA. Since the PWM signal output by the FPGA is challenging to keep consistent with the actual calculated CC operating frequency, the input impedance angle will have a slight inductive offset. Figure 26(d) shows that the input impedance angle is capacitive with different loads. The maximum capacitive angle of the input impedance is approximately $-14.82°$ when the load is 55 Ω. It is easy for the input current modeling analysis under the CV operating frequency, and the inverter realizes the ZVS. Figure 26(d) shows that the input impedance angle is capacitive with different loads. The maximum inductive angle of the input impedance is approximately 41.85° when the load is 55 Ω. It is easy for the input current modeling analysis under the CV operating frequency, and the inverter realizes the ZVS.

A. EXPERIMENTAL RESULTS OF THE INPUT IMPEDANCE ARE CAPACITIVE

The compensation network parameters are in Table 4. Figure 27(a) is the input voltage and current waveforms when the output power is 500W; Figure 27(b) is the input voltage and current waveform when the output power is 1KW. The system achieves nearly ZPA at the CC operating frequency of 1KW and 500W.

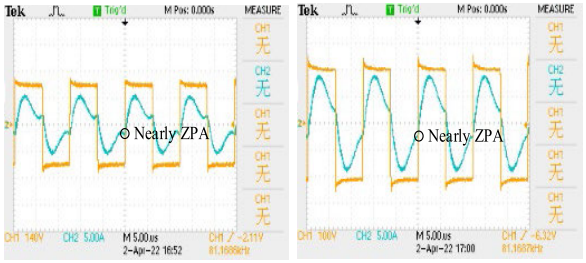

FIGURE 27. (a) Voltage and current of the system at CC frequency with the output power 500W (b)Voltage and current of the system at CC frequency with the output power 1KW.

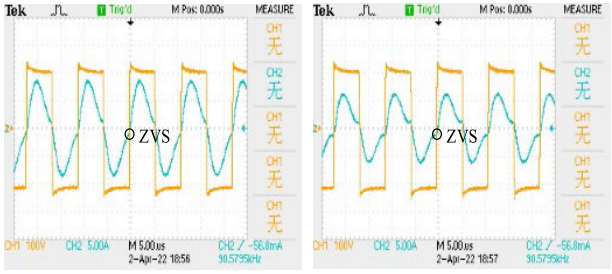

FIGURE 28. (a)Input voltage and current of the system at CV frequency with the output power of 500W (b)Input voltage and current of the system at CV frequency with the output power of 1KW.

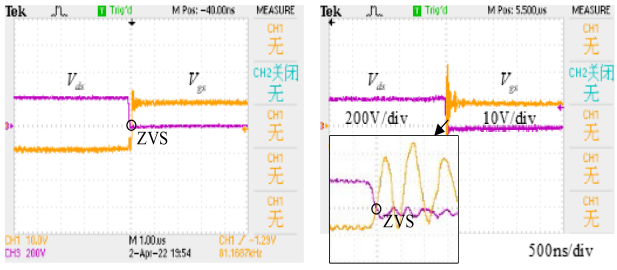

FIGURE 29. (a) Gate source and drain-source voltage of MOS at CC frequency (b) Gate source and drain-source voltage of MOS at CV frequency.

Figure 28(a) is the input voltage and current waveforms when the output power is 500W; Figure 28(b) is the input voltage and current waveform when the output power is 1KW. The system achieves nearly ZPA at the CV operating frequency of 1KW and 500W.

It can be seen from figure 27 that at the CC operating frequency, the input voltage and current are almost in phase, and the input impedance of the system is purely resistive. From figure 28, the input current waveform leads to the input voltage waveform, which is consistent with the previous analysis in this paper.

Figure 29(a) and (b) show the gate-source V_{gs} and drain-source voltage V_{ds} waveforms of MOSFET in the inverter under the CC/CV operating frequency. The ZVS of the MOSFET is realized by reducing V_{ds} to the on-state voltage drop of the MOSFET when $V_{gs} = 0$. The WPT system realizes the ZVS under the CC/CV operating frequency.

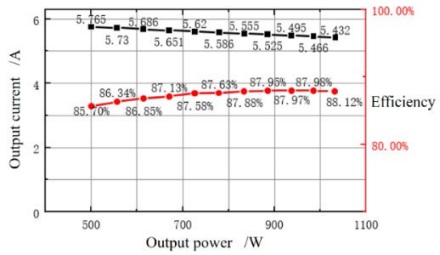

FIGURE 30. Output current and efficiency with power at CC frequency.

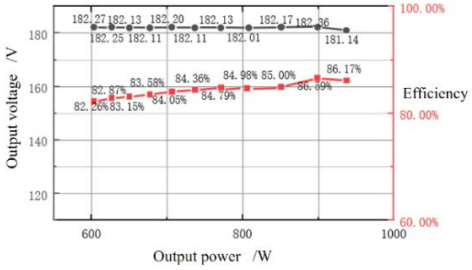

FIGURE 31. Output current and efficiency with power at CV frequency.

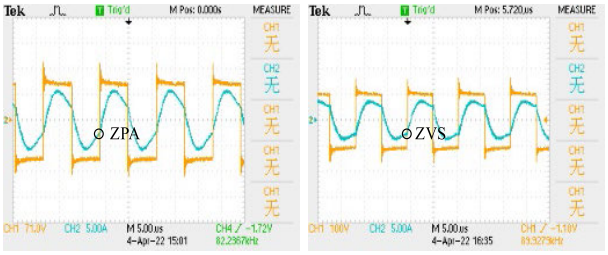

(a) (b)

FIGURE 32. (a) Input voltage and current of the system at CC frequency with the output power of 350W (b) Input voltage and current of the system at CV frequency with the output power of 250W.

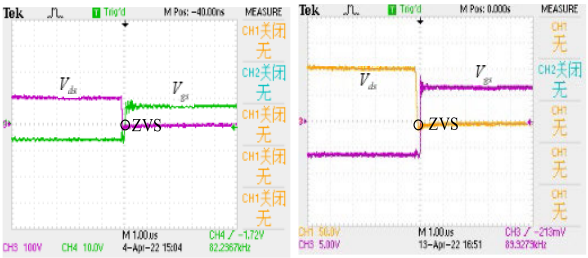

(a) (b)

FIGURE 33. (a) Gate source and drain-source voltage of MOS at CC frequency (b) Gate source and drain-source voltage of MOS at CV frequency.

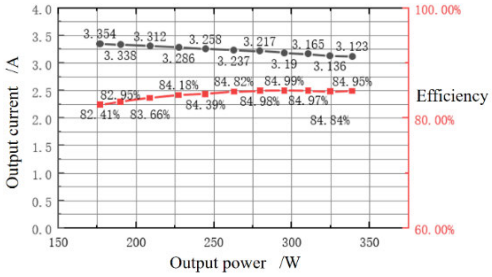

FIGURE 34. Variation curve of output current and efficiency with power at the CC frequency.

With the change of the output power, the output current of the system under the constant current operating frequency decreases with the increase of the power, but the change is not significant, which can be approximated as the constant current output. The main reasons for the change of the output current are: the deviation between the constant current operating frequency and the actual calculated value will affect the constant output characteristics; the existence of the parasitic resistance of the coil affects the constant current output; there are errors in the theoretical calculation and experimental parameters of the compensation network parameters and coil parameters; rectification Bridge diode on-state voltage drop and the presence of on-state resistance. It is found that the system's efficiency increases with the increase in output power. With the change in the output power, the system's output voltage under the constant voltage operating frequency decreases with the increase of the output power and is almost constant. The system efficiency increases with the output power increase but decreases when the load is 41 Ω (the output power is 856W). The system worked too long in the measurement, and the measurement continued after about 20 minutes. The capacitor device, the rectifier bridge, and the output filter capacitor overheat, resulting in a drop in efficiency. The system's efficiency at constant voltage and current operating frequency is not very high. The main reason for the low efficiency is that the degree of integration of the system is not enough, and the use of terminal lugs, and the use of terminal blocks and bolts, result in an extensive line impedance in the system.

V. EXPERIMENTAL RESULTS OF THE INPUT IMPEDANCE ARE INDUCTIVE

The compensation network parameters are in Table 5. The input voltage and current waveforms at CC operating frequency when the output power is 350W is in figure 32(a). The input voltage and current waveforms at CV operating frequency when the output power is 250W is in figure 32(b).

It can be seen from figure 32(a) that the input voltage and current are almost in phase at CC operating frequency. The input impedance of the system is pure resistance at CC operating frequency. Figure 32(b) shows that the input current waveform lags the input voltage waveform. The system is inductive at CV operating frequency, which is consistent with the previous analysis in this paper.

Figures 33(a) and (b) show the waveforms of the gate-source V_{gs} and drain-source voltage V_{ds} of the MOSFET in the inverter under CC/CV operating frequency. It can be seen from figure 33 that the system can realize the ZVS of MOSFET under the working frequency of CC/CV.

Under the CC operating frequency, as the system's output power increases, the system's output current decreases; under the CV operating frequency, as the system's output power increases, the system's output voltage decreases. When the system works at the CV operating frequency, the system's

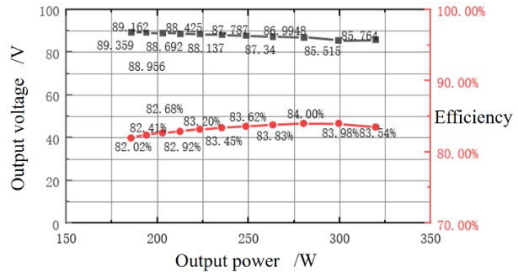

FIGURE 35. Variation curve of output current and efficiency with power at CV frequency.

efficiency is low because the input impedance of the system is inductive, and the reactive power circulating current in the system is considerable, so the efficiency is low.

VI. CONCLUSION

This paper synthesizes eight conditions that make the double-sided LCC wireless power transfer System realize CC/CV and input ZPA, a parameter design method for improving the anti-offset capability of the double-sided LCC compensation network under CC/CV and input ZPA is proposed. The influence of the variation of the series/parallel compensation capacitance of the compensation network on the input phase angle of the system is analyzed under the CC and CV operating modes, respectively, the allowable range of ZVS characteristic compensation capacitance under CC/CV operation mode is given quantitatively. The experimental results show that the ZVS characteristics of inverter switches can be achieved in CC/CV operating mode within the range of compensation capacitance.

REFERENCES

[1] Z. Yan, B. Song, Y. Zhang, K. Zhang, Z. Mao, and Y. Hu, "A rotation-free wireless power transfer system with stable output power and efficiency for autonomous underwater vehicles," *IEEE Trans. Power Electron.*, vol. 34, no. 5, pp. 4005–4008, May 2019.

[2] J. Pries, V. P. N. Galigekere, O. C. Onar, and G.-J. Su, "A 50-kW three-phase wireless power transfer system using bipolar windings and series resonant networks for rotating magnetic fields," *IEEE Trans. Power Electron.*, vol. 35, no. 5, pp. 4500–4517, May 2020.

[3] J. Shin, "Design and implementation of shaped magnetic-resonance-based wireless power transfer system for roadway-powered moving electric vehicles," *IEEE Trans. Ind. Electron.*, vol. 61, no. 3, pp. 1179–1192, Apr. 2014.

[4] C. Cheng, "Load-independent wireless power transfer system for multiple loads over a long distance," *IEEE Trans. Power Electron.*, vol. 34, no. 9, pp. 9279–9288, Sep. 2019.

[5] H. Zhu, B. Zhang, and L. Wu, "Output power stabilization for wireless power transfer system employing primary-side-only control," *IEEE Access*, vol. 8, pp. 63735–63747, 2020.

[6] J. Lu, G. Zhu, D. Lin, Y. Zhang, H. Wang, and C. C. Mi, "Realizing constant current and constant voltage outputs and input zero phase angle of wireless power transfer systems with minimum component counts," *IEEE Trans. Intell. Transp. Syst.*, vol. 22, no. 1, pp. 600–610, Jan. 2021.

[7] X. Zhu, "High-efficiency WPT system for CC/CV charging based on double-half-bridge inverter topology with variable inductors," *IEEE Trans. Power Electron.*, vol. 37, no. 2, pp. 2437–2448, Feb. 2022.

[8] V. Yenil and S. Cetin, "Load independent constant current and constant voltage control of LCC-series compensated wireless EV charger," *IEEE Trans. Power Electron.*, vol. 37, no. 7, pp. 8701–8712, Jul. 2022.

[9] M. Kim, D.-M. Joo, and B. K. Lee, "Design and control of inductive power transfer system for electric vehicles considering wide variation of output voltage and coupling coefficient," *IEEE Trans. Power Electron.*, vol. 34, no. 2, pp. 1197–1208, Feb. 2019.

[10] J. Liu, C. S. Wong, C. Sun, F. Xu, X. Jiang, and K. H. Loo, "Software-reconfigurable multistage constant current wireless battery charging based on multiharmonic power transmission," *IEEE Trans. Power Electron.*, vol. 38, no. 4, pp. 5586–5597, Apr. 2023, doi: 10.1109/TPEL.2022.3232704.

[11] A. Vulfovich and A. Kuperman, "Design space of sub-resonant frequency-controlled series–series-compensated inductive wireless power transfer links operating with constant output current under frequency constraints," *IEEE J. Emerg. Sel. Topics Power Electron.*, vol. 10, no. 5, pp. 5414–5422, Oct. 2022, doi: 10.1109/JESTPE.2022.3179724.

[12] J. Hou, Q. Chen, L. Zhang, L. Xu, S.-C. Wong, and C. K. Tse, "Compact capacitive compensation for adjustable load-independent output and zero-phase-angle input for high efficiency IPT systems," *IEEE J. Emerg. Sel. Topics Power Electron.*, vol. 10, no. 4, pp. 4923–4936, Aug. 2022, doi: 10.1109/JESTPE.2022.3140593.

[13] Y. Yang, S.-C. Tan, and S. Y. R. Hui, "Front-end parameter monitoring method based on two-layer adaptive differential evolution for SS-compensated wireless power transfer systems," *IEEE Trans. Ind. Informat.*, vol. 15, no. 11, pp. 6101–6113, Nov. 2019, doi: 10.1109/TII.2019.2924926.

[14] K. Song, Z. Li, J. Jiang, and C. Zhu, "Constant current/voltage charging operation for series-series and series-parallel compensated wireless power transfer systems employing primary-side controller," *IEEE Trans. Power Electron.*, vol. 33, no. 9, pp. 8065–8080, Sep. 2018, doi: 10.1109/TPEL.2017.2767099.

[15] X. Qu, H. Chu, Z. Huang, S. C. Wong, K. T. Chi, C. C. Mi, and X. Chen, "Wide design range of constant output current using double-sided LC compensation circuits for inductive-power-transfer applications," *IEEE Trans. Power Electron.*, vol. 34, no. 3, pp. 2364–2374, May 2018.

[16] A. Ramezani, S. Farhangi, H. Iman-Eini, B. Farhangi, R. Rahimi, and G. R. Moradi, "LCC-series compensated resonant network for stationary wireless EV chargers," *IEEE Trans. Ind. Electron.*, vol. 66, no. 4, pp. 2756–2765, Apr. 2019.

[17] J. Hou, Q. Chen, Z. Zhang, S.-C. Wong, and C. K. Tse, "Analysis of output current characteristics for higher order primary compensation in inductive power transfer systems," *IEEE Trans. Power Electron.*, vol. 33, no. 8, pp. 6807–6821, Aug. 2018.

[18] S. Li, W. Li, J. Deng, T. D. Nguyen, and C. C. Mi, "A double-sided LCC compensation network and its tuning method for wireless power transfer," *IEEE Trans. Veh. Technol.*, vol. 64, no. 6, pp. 2261–2273, Jun. 2015, doi: 10.1109/TVT.2014.2347006.

[19] B. M. Mosammam and M. Mirsalim, "New integrated tripolar pad using double-sided LCC compensation for wireless power transfer," *IEEE Trans. Veh. Technol.*, vol. 69, no. 12, pp. 15633–15643, Dec. 2020, doi: 10.1109/TVT.2020.3045371.

[20] X. Qu, H. Chu, S.-C. Wong, and C. K. Tse, "An IPT battery charger with near unity power factor and load-independent constant output combating design constraints of input voltage and transformer parameters," *IEEE Trans. Power Electron.*, vol. 34, no. 8, pp. 7719–7727, Aug. 2019.

[21] V.-B. Vu, D.-H. Tran, and W. Choi, "Implementation of the constant current and constant voltage charge of inductive power transfer systems with the double-sided LCC compensation topology for electric vehicle battery charge applications," *IEEE Trans. Power Electron.*, vol. 33, no. 9, pp. 7398–7410, Sep. 2018.

[22] C. Jin and W. Xusheng, "Stability analysis and efficiency optimization design of bilateral LCC inductively coupled power transmission system," *Trans. China Electrotech. Soc.*, vol. 35, no. 2, pp. 355–362, 2020.

[23] D. Li, X. Wu, J. Gao, J. Lu, and W. Gao, "Sensitivity analysis and parameter optimization of inductive power transfer," *IEEE Access*, vol. 9, pp. 166951–166961, 2021.

[24] H. Hu, T. Cai, S. Duan, X. Zhang, J. Niu, and H. Feng, "An optimal variable frequency phase shift control strategy for ZVS operation within wide power range in IPT systems," *IEEE Trans. Power Electron.*, vol. 35, no. 5, pp. 5517–5530, May 2020.

[25] Y. Guo, L. Wang, Y. Zhang, S. Li, and C. Liao, "Rectifier load analysis for electric vehicle wireless charging system," *IEEE Trans. Ind. Electron.*, vol. 65, no. 9, pp. 6970–6982, Sep. 2018.

DA LI was born in Wuhan, Hubei, in 1994. He is currently pursuing the Ph.D. degree in electrical engineering with the School of Electrical Engineering, Naval University of Engineering.

His research interests include wireless power transmission, RFID technology and its applications, and antenna design.

XUSHENG WU was born in Pujiang, Zhejiang, in 1976. He received the Ph.D. degree in electrical engineering from the Naval University of Engineering, in 2003.

He worked in the postdoctoral research station in electrical engineering with Wuhan University, from 2004 to 2007. His research interests include power integration technology and wireless power transmission.

CHUNYANG AN was born in Ningliao, China, in 1997. He received the master's degree in electrical engineering from the Naval University of Engineering, in 2021.

His research interest includes wireless power transmission.

JIANXIN GAO was born in Zibo, Shandong, in 1989. He received the Ph.D. degree in electrical engineering from the Naval University of Engineering, in 2017.

His research interests include wireless power transmission and UAV technology and applications.

WEI GAO was born in Zibo, Shandong, in 1980. He received the Ph.D. degree in electrical engineering from the Naval University of Engineering, in 2011.

He worked in the postdoctoral research station with the 28th Research Institute of Electronic Technology Group. His research interests include wireless power transmission and electrical machinery and appliances.